Single-spin sensing of domain-wall structure and dynamics in a thin-film skyrmion host

Alec Jenkins, Matthew Pelliccione, Guoqiang Yu, Xin Ma, Xiaoqin Li, Kang L. Wang, and Ania C. Bleszynski Jayich

Phys. Rev. Materials **3**, 083801 — Published 1 August 2019

DOI: 10.1103/PhysRevMaterials.3.083801

Single spin sensing of domain wall structure and dynamics in a thin film skyrmion host

Alec Jenkins,[1] Matthew Pelliccione,[1] Guoqiang Yu,[2] Xin Ma,[3]
Xiaoqin Li,[4] Kang L. Wang,[5] and Ania C. Bleszynski Jayich[1]

[1]*Department of Physics, University of California, Santa Barbara, Santa Barbara, California 93106, USA*
[2]*Beijing National Laboratory for Condensed Matter Physics, Institute of Physics, Chinese Academy of Sciences, Beijing 100190, China*
[3]*Department of Electrical and Computer Engineering, University of California, Santa Barbara, Santa Barbara, California 93106, United States*
[4]*Department of Physics, The University of Texas at Austin, Austin, Texas 78712, United States*
[5]*Department of Electrical Engineering, University of California, Los Angeles, California 90095, United States*

(Dated: July 8, 2019)

Skyrmions are nanoscale magnetic structures with features promising for future low-power memory or logic devices. In this work, we demonstrate novel scanning techniques based on nitrogen vacancy center magnetometry that simultaneously probe both the magnetic dynamics and structure of room temperature skyrmion bubbles in a thin film system Ta/CoFeB/MgO. We confirm the handedness of the Dzyaloshinskii-Moriya interaction in this material and extract the magnitude of the helicity angle of the skyrmion bubbles. Our measurements also show that the skyrmion bubbles in this material change size in discrete steps, dependent on the local pinning environment, with their average size determined dynamically as their domain walls hop between pinning sites. In addition, an increase in magnetic field noise is observed near skyrmion bubble domain walls. These measurements highlight the importance of interactions between internal degrees of freedom of skyrmion bubble domain walls and pinning sites in thin film systems. Our observations have relevance for future devices based on skyrmion bubbles where pinning interactions will determine important aspects of current-driven motion.

I. INTRODUCTION

Magnetic skyrmions are solitonic spin textures with non-trivial topology. They were first discovered in non-centrosymmetric bulk crystals and ultrathin epitaxial magnetic layers [1–4]. The skyrmions observed in those materials had nanoscale sizes and large current-driven velocities, leading to their identification as promising candidates as carriers of information in future high-density, low-power electronics [5–8]. Recently, much interest has focused on the creation of related magnetic structures in sputtered thin film multilayers [9–12]. These multilayer materials are promising for making practical skyrmion devices, but further materials development is required to achieve the 10 nm-scale and efficient current-driven motion desired for applications [13].

As skyrmion multilayers and devices are developed, local, real-space probes of these systems will be crucial to understanding their microscopic behavior. Measurements of skyrmion size and structure, current-driven behavior, and interaction with defects will be necessary to engineer materials with characteristics optimized for use in skyrmion devices. Several imaging techniques have already been used to study skyrmions, including Kerr microscopy [10, 14], Lorentz transmission electron microscopy [15, 16], transmission X-ray microscopy [9, 17, 18], and magnetic force microscopy [12, 19, 20]. While each of these tools has certain advantages, a scanning probe microscope (SPM) based on the nitrogen-vacancy (NV) defect in diamond [21–23] is another probe particularly well-suited to studying skyrmion devices; the NV-SPM is magnetically non-invasive and offers quantitative, nanoscale spatial resolution of stray magnetic fields over a wide range of temperatures and magnetic fields [24–29].

In this work, we utilize a scanning NV microscope to study bubble skyrmions [30], in the multilayer system $Ta(2nm)/Co_{20}Fe_{60}B_{20}(1nm)/Pt(1Å)/MgO(2nm)$ [10]. We demonstrate that scanning NV microscopy is a uniquely versatile tool for the study of skyrmion materials, useful for investigating both magnetic structure and dynamics in these materials. Specifically, we use the NV microscope to extract magnetic parameters of this thin film system such as the exchange stiffness and the domain wall width and then employ these parameters to study the chiral nature of the skyrmion spin structure. Importantly, our measurements show ubiquitous interactions between pinning sites and the internal degrees of freedom of skyrmion bubble domain walls. Pinning of skyrmion internal degrees of freedom has previously been shown to be a key factor in determining skyrmion size in similar multilayer systems [17, 18, 29]. Here, we observe that skyrmion bubble sizes change in discrete steps as a function of the applied external field. For many of the observed skyrmion bubbles, their average size is determined dynamically as sections of the bubble domain walls hop back and forth between multiple pinning sites. We quantitatively probe the dynamics of these hopping processes using spectroscopy of an NV center positioned near fluctuating bubble walls. We also observe switching in real time between bubble and saturated ferromagnetic states, and we image the local magnetic noise environment near skyrmion

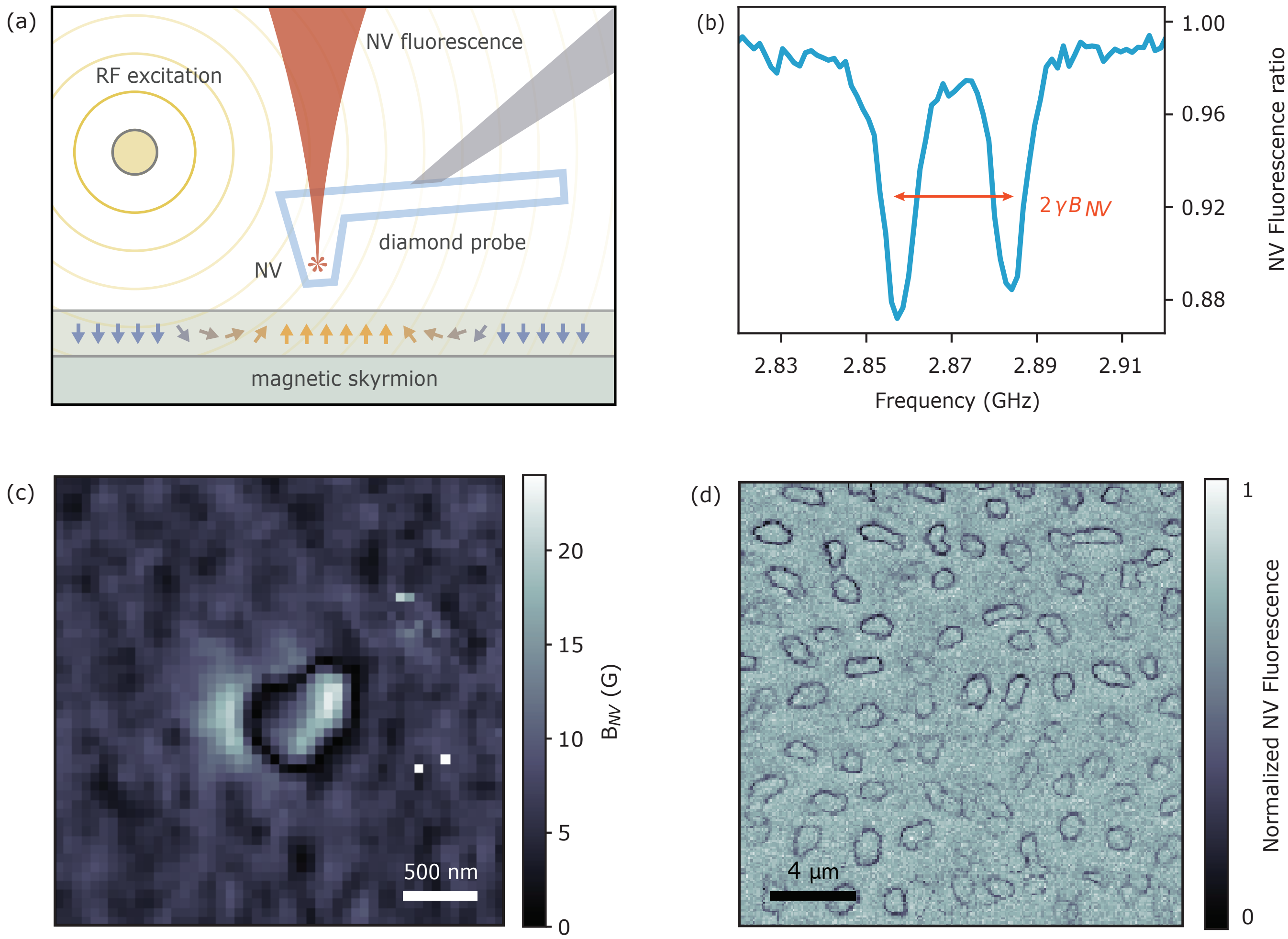

FIG. 1. Scanning NV-based imaging of skyrmions. (a) Diagram of the experimental setup. A single-crystal diamond probe containing a single NV center near the apex of its tip is scanned above the multilayer sample. Simultaneous optical and RF excitation of the NV gives an ESR signal (b), which is used to measure the stray magnetic field at each position in the scan. (b) Example of an NV ESR signal: the NV fluorescence rate decreases when applied microwaves are on resonance with either of the NVs two spin transitions ($m_s = 0 \rightarrow +1$ and $m_s = 0 \rightarrow -1$). The splitting of the two peaks is used to calculate B_{NV}, the magnetic field along the NV center axis. Plotted is the ratio of the NV fluorescence to its off-resonant value. (c) NV magnetic image of a skyrmion bubble with an external magnetic field of 10.0 Oe perpendicular to the film plane. (d) Magnetic contour image with applied microwave frequency = 2.870 GHz and with 6.5 Oe perpendicular to the film plane.

bubbles and observe an increase in magnetic noise near skyrmion bubble domain walls. Our direct observations of skyrmion bubbles interacting with multiple pinning sites have important implications for skyrmion bubble motion in this material. As shown previously, high densities of pinning sites can lead to a break down of typical micromagnetic models of skyrmion motion, which show low depinning current densities and large velocities in the presence of sparse defects [9].

II. EXPERIMENTAL SETUP

In these measurements, a single NV center in a diamond probe is scanned over the sample surface while the stray magnetic field is measured using the NV center's optically detected magnetic resonance spectrum (Fig. 1), hence referred to as its (electron spin resonance) ESR spectrum [28]. This spectrum is measured by sweeping the frequency of applied microwaves while monitoring the spin-state-dependent NV fluorescence rate (Fig. 1b). Magnetic fields induce a Zeeman splitting Δf between the NV $m_s = \pm 1$ spin states that is proportional to the absolute value of the stray field along the axis of the NV— $\Delta f \simeq 2\gamma |B_{NV}|/(2\pi)$, where $\gamma = 2\pi \times 2.8$ MHz/G is the gyromagnetic ratio of the NV. B_{NV} is calculated for a given ESR spectrum using this Zeeman splitting with a small correction due to fields perpendicular to the NV axis [31]. ESR measurements are used to acquire a two-dimensional map of B_{NV} (Fig. 1c). Based on this map, it is possible to reconstruct all vector components of the stray field [32, 33], and the reconstructed vector

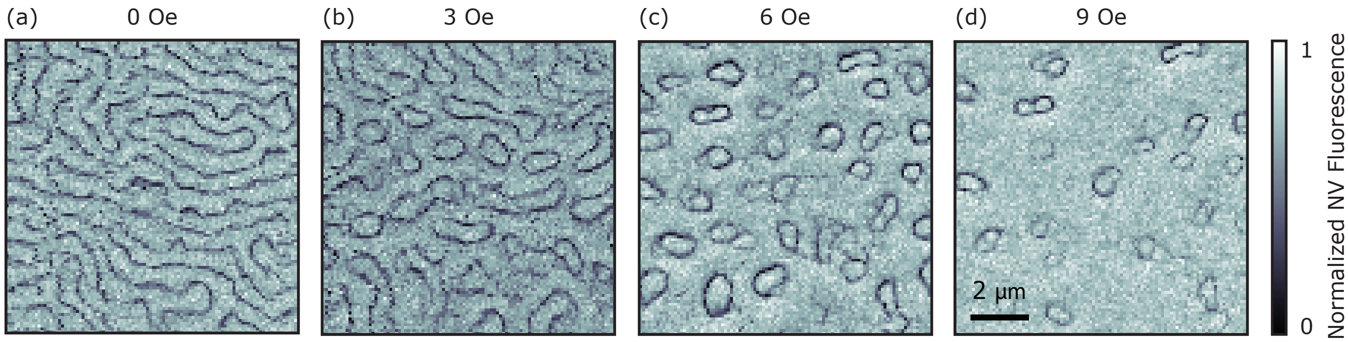

FIG. 2. Field contour images of magnetic phases in Ta/CoFeB/MgO system acquired with the NV microscope. The applied microwave frequency is 2.870 GHz for all images. An external magnetic field applied normal to the sample plane is increased from 0-9 Oe in (a)-(d). As the field increases, the magnetic order evolves from stripes at 0 Oe (a) into a mixed skyrmion/stripe phase at 3 Oe (b) and a skyrmion phase at 6 (c) and 9 (d) Oe. At these fields, zero-field contours mark the approximate domain wall positions. The scale bar for all images is shown in (d).

field can be used to estimate the domain wall positions comprising an individual magnetic bubble and probe the internal structure of domain walls [26, 27, 34]. The imaging resolution of this technique is determined by the distance from the NV to the magnetic CoFeB layer. For the image in Fig. 1c, this distance was measured to be 58 ± 5 nm [35].

Measuring the ESR spectrum at each scan point is time intensive, so a faster contour imaging method is used to get information about magnetic structure. In a contour measurement, the frequency of applied microwaves is fixed while the microwave amplitude is square-wave modulated on/off at kHz frequencies. The NV fluorescence rate difference for microwaves on vs. off is measured at each point of the scan. Dark contours in the resulting image correspond to resonances of the applied microwaves with the $m_s = 0$ to $m_s \pm 1$ transitions— to first order giving contours of constant magnetic field. These contours, with a properly chosen microwave frequency, correspond to domain wall locations in the underlying thin film, as discussed below. The contour image in Fig. 1d outlines the approximate domain wall positions of a group of skyrmion bubbles.

III. MAGNETIC PHASES Ta/CoFeB/MgO

In the Ta/CoFeB/MgO thin film system, perpendicular magnetic anisotropy (PMA) due to the CoFeB/MgO interface allows for the existence of magnetic bubbles stabilized under a small magnetic field perpendicular to the film. An interfacial Dzyaloshinskii-Moriya interaction (DMI) arising from an antisymmetric exchange coupling at the interface of the ferromagnetic CoFeB and strong spin-orbit Ta layers encourages a fixed chirality of the magnetization structure of these bubbles. A wedged sub-nm Pt insertion layer between the CoFeB and MgO tunes the PMA strength by weakening Co-O and Fe-O bonds at the MgO interface. This Pt insertion layer also induces a DMI at the top CoFeB interface, modifying the total DMI strength [36–38]. A magnetic field B_{ext} is applied perpendicular to the sample plane giving rise to isolated skyrmions in certain regions of the PMA-B_{ext} phase space [10]. The NV fluorescence images in Fig. 2 show the evolution of the magnetic order with B_{ext}. At $B_{ext} = 0$, magnetic order takes the form of stripe-like domains. As B_{ext} is increased, the system undergoes a first order phase transition into a skyrmion phase. In Fig. 2, a coexistence of skyrmion bubbles and stripes is seen already at 3 Oe, and several bubbles persist up to $B_{ext} = 9$ Oe. At fields larger than 10 Oe, the material transitions into a ferromagnetic phase with no magnetic features in the NV images. The images in Fig. 2 were obtained using the contour imaging method, with the frequency of the applied microwaves fixed to the NV zero-field splitting frequency of 2.870 GHz. For the small values of B_{ext} used, the dark contours mark the approximate domain wall positions, with a small (< 100 nm) scale offset in the direction of the NV's in-plane projection [35]. The width of the contour lines, which can be much smaller than the NV-sample separation, is determined by the width of the NV ESR dip and the magnetic field gradients near the domain walls [39].

IV. SKYRMION BUBBLE PINNING DYNAMICS

The high resolution of the NV center scanning microscope allows for the study of the microscopic structure of these bubble domains [26, 27]. For example, contour images of domain wall position show the effects of pinning sites on skyrmion shape (Fig. 3a), which induce both a static deformation of the skyrmion as well as a dynamic instability. Figures 2c-d and the higher resolution contour images in Fig. 3a-g show irregularly shaped skyrmions, whose dramatic deviation from a disorder-free, circular shape is consistent with previously reported

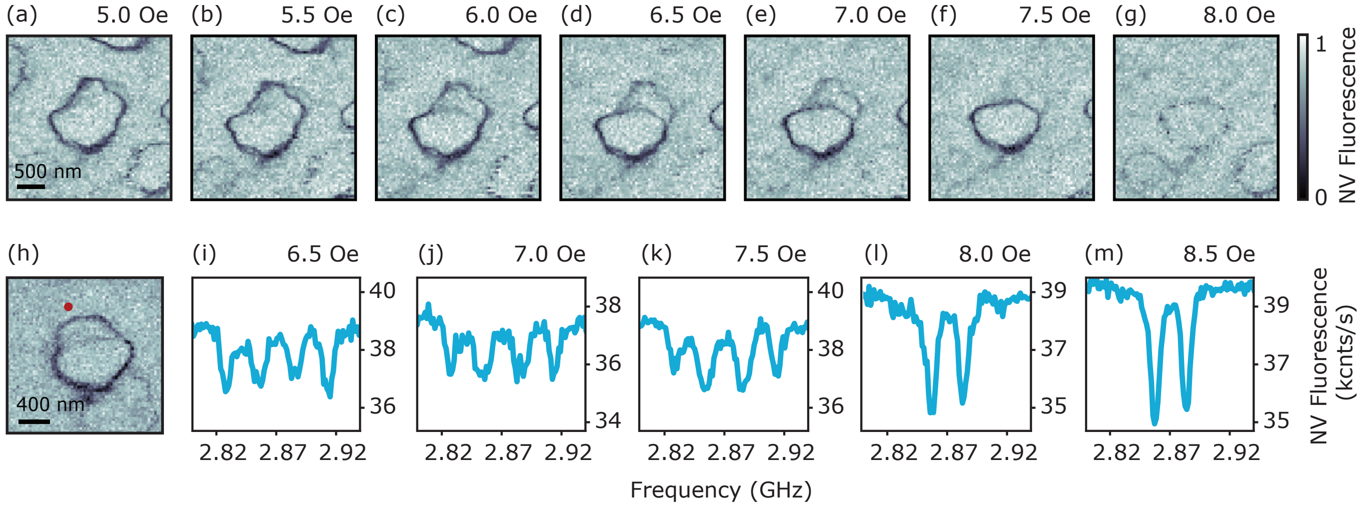

FIG. 3. Domain wall fluctuations and evolution with B_{ext} imaged by NV center microscopy. (a) 2.870 GHz contour images of a skyrmion bubble, each labeled by the corresponding B_{ext} applied during that scan. As B_{ext} increases, a section of the domain wall evolves into a bistable configuration, seen most clearly in the (d) and (e) scans with 6.5 and 7.0 Oe. The scale bar for (a)-(g) is shown in (a). (h) 2.870 GHz contour images of another skyrmion bubble taken at $B_{ext} = 7.0$ G. (i)-(m) NV center ESR spectra taken with the NV fixed at the location indicated by the red dot, each labeled by B_{ext}. The mulitple pairs of ESR splittings in each spectrum correspond to different positions of the domain wall.

NV-microscopy images of a similar thin film magnetic multilayer [29]. The effect of pinning sites is also manifest in the evolution of skyrmion size and shape with magnetic field, as shown in Fig. 3. When B_{ext} is increased from 5 to 7.5 Oe the skyrmion shrinks, as seen by comparing Fig. 3a and 3f and as predicted by micromagnetic theory [40]. Interestingly, however, this process does not happen smoothly but rather discontinuously: at intermediate fields in the range of $B_{ext} = 6.0$–7.5 Oe, the images in Fig. 3b-e show domain wall contours corresponding to both the larger and smaller diameter skyrmion. As the field is increased, the contrast of the larger diameter contour progressively decreases while the contrast of the smaller diameter contour increases. This behavior is explained by the domain wall hopping back and forth in time between two stable positions, progressively spending a larger fraction of its time in a smaller diameter configuration as the field is increased. Hopping that occurs on a timescale faster than the NV measurement leads to a reduction in the contrast of the contours because the NV fluorescence signal is averaged over its bright and dark states as the fluctuating field produced by the hopping domain wall brings the applied microwaves on and off resonance with the NV ESR transitions. Thus, although our measurement is too slow to detect the telegraph nature of the domain wall hopping in real time, we can detect time-averaged signatures of the dynamics through changes in contour contrast.

We can confirm the time-averaged behavior of the domain wall fluctuations by fixing the NV at a location near a fluctuating domain wall while recording the ESR spectrum, as shown in Fig. 3i-m. The position of the NV is indicated by the red dot in Fig. 3h. In the spectrum, the hopping of the domain wall appears as two dominant ESR splittings that emerge as the magnetic field is swept through the skyrmion phase. When the domain wall is near the NV, the ESR splitting is largest, given by the outer two ESR dips. The existence of other ESR dips in the spectra in Fig. 3 implies that the domain wall spends some time at another position, seen as the faint contour line cutting across the middle of the bubble in Fig. 3h. Qualitatively, the evolution of the contrast ratio between different pairs of dips in the ESR spectrum or equivalently, between domain wall branches in the contour images, gives an indication of the relative time spent in different domain wall states. As B_{ext} is increased, the outer pair of ESR dips grows fainter as the domain wall evolves from spending more time in the larger skyrmion diameter configuration (near the NV) to spending more time in the small diameter configuration. At $B_{ext} = 8.5$ Oe, the skyrmion bubble is no longer stable and the ESR splitting is given by the NV-axis projection of B_{ext}.

Importantly, our NV imaging technique allows us to glean quantitative information about the time scale of the domain wall dynamics. We estimate the average hopping rate, χ, of the domain wall in Fig 3h to lie in the range of tens of Hz to tens of MHz by making the following two observations. First, telegraph switching of the NV fluorescence rate was not observed on time scales slower than 0.01 seconds, putting a lower bound on χ. In this experiment, we could not explore faster time scales because of insufficient signal to noise ratio for smaller measurement time bins. An upper limit on the characteristic hopping frequency can be set by treating the domain wall position between the two pinning sites as a quasi-1D system and assuming that the dynamics is governed by an Ar-

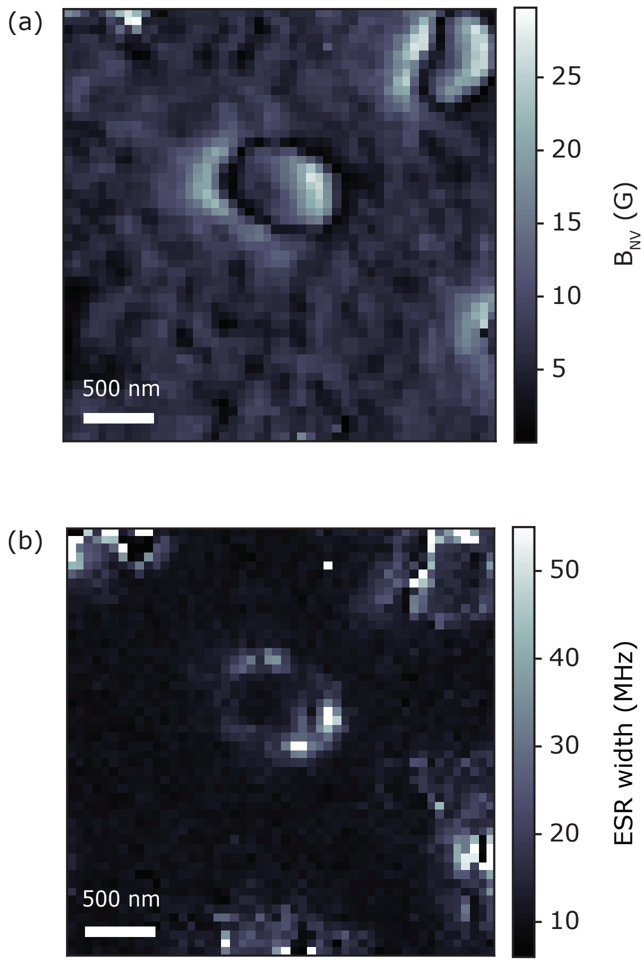

FIG. 4. Enhanced magnetic fluctuations near skyrmion domain walls (a) Spatial map of the magnetic field along the NV axis. The external field, $B_{ext} = 9.5$ Oe, is normal to the film plane. (b) NV ESR width averaged over both ESR dips, showing enhanced mangetic fluctuations at the skyrmion domain wall.

rhenius type thermal activation of hopping between two sites [41], where the number of domain wall jumps in a given time is described by a Poisson process. In this case, the NV ESR spectrum is expected to take two different forms, displaying either a single resonance line or a split pair of resonance lines for each spin transition, depending on the characteristic rate of domain wall hopping χ and the corresponding spectral shift of the NV ESR dip. Focusing on one NV spin transition, for example $m_s = 0 \rightarrow -1$, the spectral shift can be written as $\Delta f_{ESR} = f_{DW2} - f_{DW1}$, where f_{DW1} and f_{DW2} are the NV resonance frequencies corresponding to the two domain wall positions. In the limit $\Delta f_{ESR} > \chi$, distinct resonances will be observed at f_{DW1} and f_{DW2}, whereas in the limit $\Delta f_{ESR} < \chi$, an effect similar to motional narrowing will give a spectrum with a single resonance at $(f_{DW2} + f_{DW1})/2$ if, on-average, an equal amount of time is spent in both domain wall positions [42, 43]. The distinct ESR lines shown in Fig. 3i indicate that the first limit applies and that the characteristic frequency of the observed domain wall hopping is limited to $\chi < 20$ MHz. This reasoning can also be applied to other observed bistable skyrmion bubble walls, for example those shown in Fig. 3c-e. Assuming that these domain wall branchings are due to a similar hopping mechanism observed in Fig. 3h and 3i, the fact that two domain wall positions are observed in Fig. 3c-e can be used to place a rough limit on the timescale of those domain wall dynamics as well.

In addition to large jumps of domain wall position that produce a discrete set of ESR splittings, we also observe magnetic fluctuations that broaden the NV spin transitions when the NV is positioned near domain walls. Fig. 4b shows a spatial map of the average ESR width with corresponding stray field measurement in Fig. 4a. Figure 4b shows that magnetic fluctuations are enhanced near the skyrmion bubble walls, even in the absence of the clear bistabilities seen in Fig 3. We note that this broadening is not due to fluctuations in the NV-domain wall distance in regions of high magnetic fields gradient, as it is not observed near other sharp magnetic features not associated with bubble domain walls [35]. The emergence of these enhanced fluctuations near domain walls is not well understood and can be interpreted in a few ways. It could imply the existence of small fluctuations in the position of all domain walls, driven thermally or magnetically [44], possibly by the applied microwaves or laser light [45]. Alternatively, the spatial dependence seen in Fig. 4b could be the result of amplification or concentration of magnetic noise sources, such as spin waves, near the domain walls [46, 47]. We note that the increase in magnetic noise at the bottom of Fig. 4b is due to fluctuations of another bubble skyrmion whose dominant domain wall position is not seen in Fig. 4a [35].

We have also observed switching dynamics between a bubble skyrmion state and a saturated ferromagnetic state, with a time scale slow enough to be observed in real time with the NV center. Figure 5a shows a skyrmion bubble contour ($B_{ext} = 9.2$) that becomes unstable as the field is increased to 9.5 G, as seen in Figs. 5b-c. Figure 5b shows a decrease in contour contrast due to switching between the bubble state and saturated ferromagnetic state. The switching dynamics can be directly observed as telegraph noise in the NV fluorescence time trace shown in Fig. 5c, obtained by fixing both the NV location (red dot in 5b) and the microwave frequency. High fluorescence corresponds to the ferromagnetic state and low fluorescence corresponds to the bubble state. The characteristic switching frequency can be extracted from the distributions of dwell times in each state. From a 30 second fluorescence trace, a characteristic switching frequency of 14 Hz is measured for both directions of state switching, implying that the energy of the two states is approximately equal at the applied field of $B_{ext} = 9.5$ G. The switching frequency is ultimately determined by the energy barrier between the bubble and saturated mag-

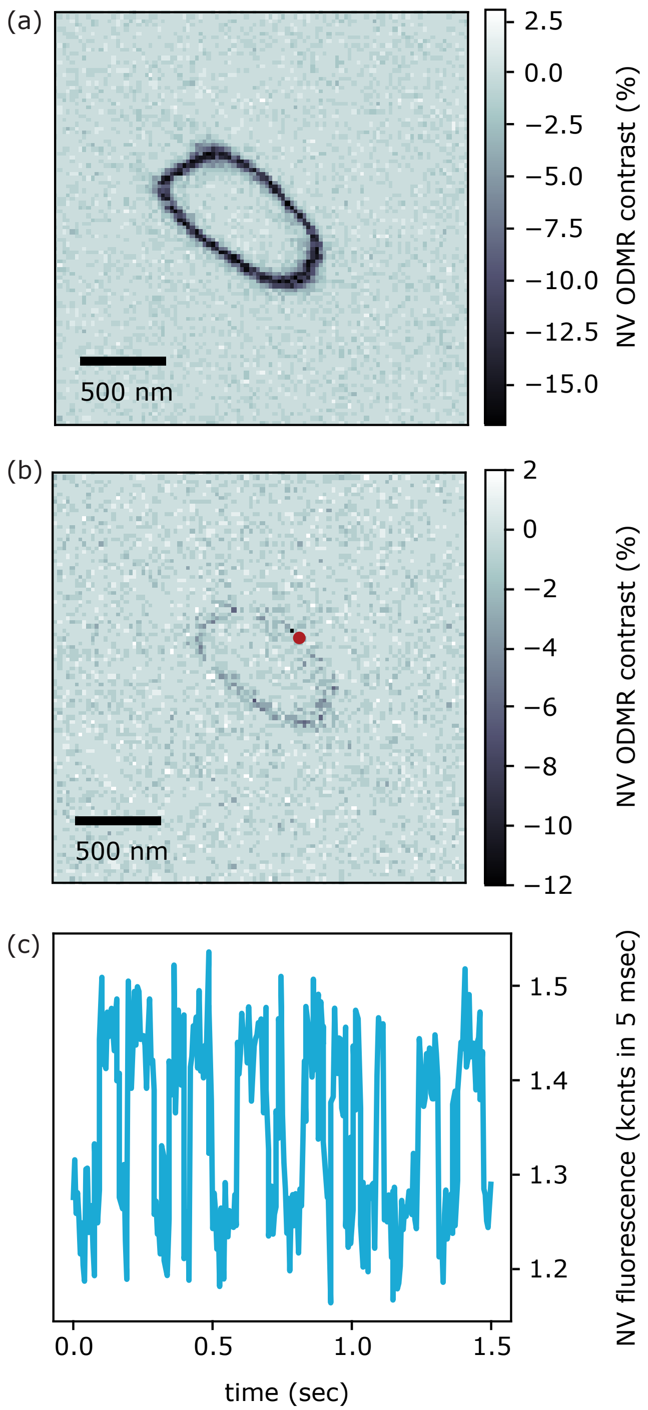

FIG. 5. Telegraph switching of the NV fluorescence signal in the presence of a skyrmion bubble switching between a bubble and a saturated state. (a) 2.870 GHz contour image of the skyrmion bubble shown in Fig. 4 taken at $B_{ext} = 9.2$ G. (b) 2.870 GHz contour image of the skyrmion bubble shown in Fig. 4 taken at $B_{ext} = 9.5$ G. As the field is increased, the bubble state becomes unstable and switching between the saturated and bubbles sates is observed as a decrease in the NV ESR contrast. (C) The ESR signal when fixing the NV position at the location indicated by the red dot in (b) with $B_{ext} = 9.5$ G. (d) The NV fluorescence collected in 5 msec bins when fixing the NV location at the position indicated by the red dot in (b), and fixing the drive microwave frequency at 2.871 GHz (the frequency indicated by the dashed red line in (c)). A characteristic hopping frequency of 14 Hz is measured over the full 30 second measurement window.

netic states. These energy barriers have been estimated previously for DMI-stabilized thin-film skyrmions [48], and the process of skyrmion collapse to a helical state has been explored in a bulk skrmion system [49]. In the present case, the bubble is dipole stabilized and the energy barrier can be estimated by a cylindrical bubble domain model [50]. Using an Arrhenius description of the switching, $f = f_0 \exp(-E_B/k_B T)$, where $E_B \simeq 240$ meV is the energy barrier in the bubble domain model, $T = 298$ K, $f = 14$ Hz is the characteristic switching frequency, the attempt frequency f_0 is determined to be $\simeq$0.35 MHz. We note, however, that local material variations may alter the energy barrier.

V. SKYRMION BUBBLE STRUCTURE

The magnetic structure of skyrmions has important implications for the viability and design of skyrmion-based devices because the structure determines important parameters of current-driven skyrmion motion, such as the skyrmion Hall angle and velocity [14, 51–53]. However, probing the structure of skyrmion bubble is difficult due to the required nanometer-scale resolution. While many techniques can be used to determine domain wall structure in principle, there are few examples of probes that are local, non-invasive, and capable of studying a wide range of skyrmion materials. Recent NV imaging studies of magnetic thin films have established scanning NV microscopy as a useful probe of magnetic structure with all these features [26, 27, 34, 54]. Starting from a map of the NV-axis stray field (Fig. 6a), a partial reconstruction of the magnetization structure is possible but requires knowledge of several material parameters, careful calibration of the NV scan height, and some structure assumptions based on micromagnetic theory. In this work, we determine all relevant materials parameters, leaving free only the absolute value of the domain wall helicity angle $|\psi_h|$. The helicity angle sets the rotation direction of magnetization through a cross-section of the domain wall— here defined relative to the common domain wall types as $|\psi_h| = 0, \pi/2$, and π for right-handed Néel, Bloch, and left-handed Néel respectively. With this approach we can use the local, nanoscale nature of the NV probe to search for variations in the helicity angle magnitude along the skyrmion domain wall, which allows us to check for a fixed chirality of individual bubbles.

We start by assigning a polarity to regions of the B_{NV} map separated by zero-field contours. The polarity direction is determined by the direction of the applied external field. This signed field map can in turn be used to calculate the full vector components of the stray magnetic field [26, 33]. The z component of $\mathbf{B}$ (where $\hat{\mathbf{z}}$ is normal to the sample) at the sample surface can be extrapolated and used to estimate the domain wall position [35]. The magnetization pattern $\mathbf{M}$ is then fully determined by the domain wall width Δ_{DW}, saturation magnetization M_s,

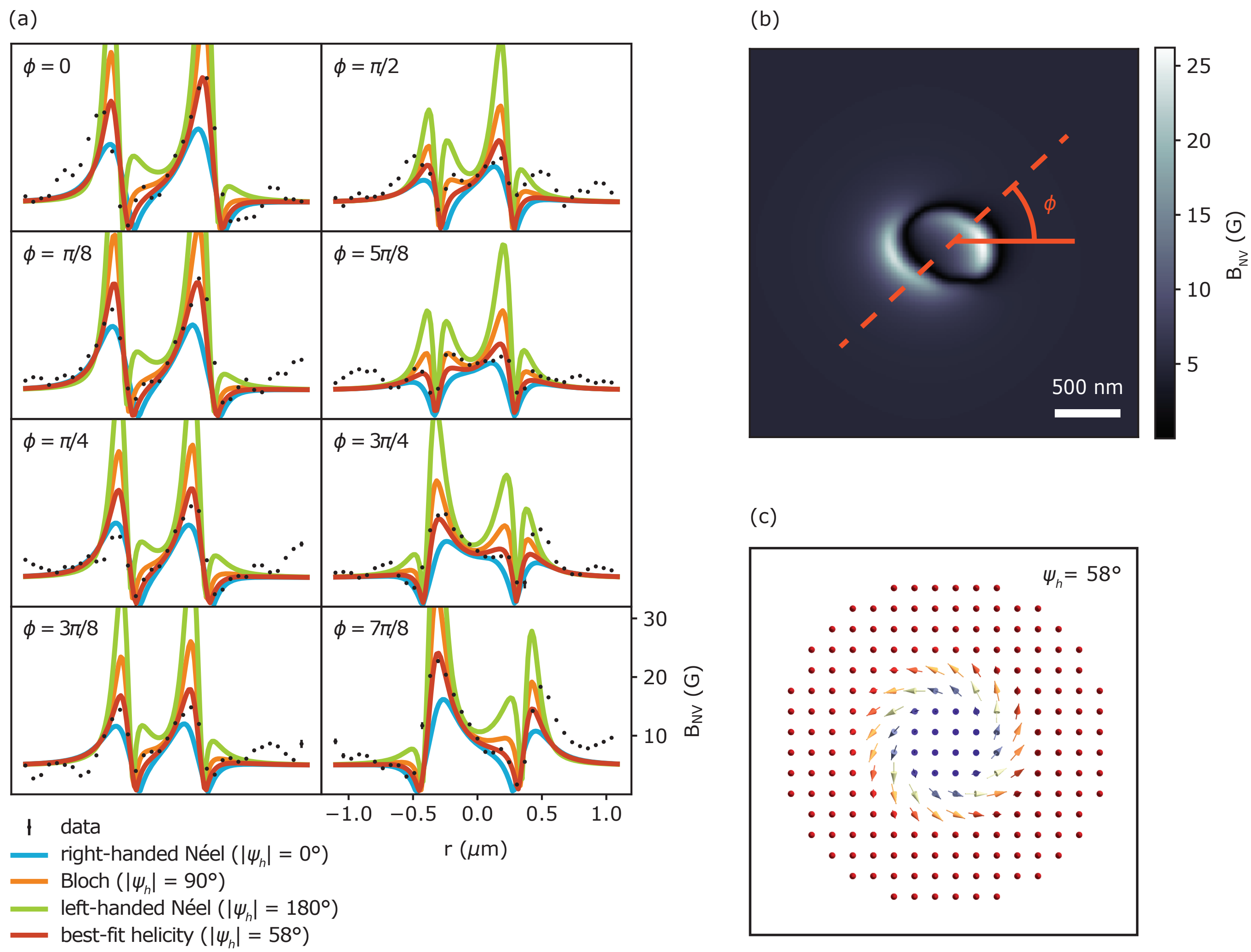

FIG. 6. Reconstruction of helicity angle. (a) Linecuts at various angles ϕ across a magnetic bubble, comparing the measured magnetic field shown in Fig. 4a to the simulated field for four domain wall types— right-handed Néel, Bloch, left-handed Néel, and a domain wall with $|\psi_h| = 58°$. The NV height is calibrated to be 58±5 nm using the method described in [35]. The NV angle relative to the film normal is measured as $60° \pm 4°$ using an external field aligned along the film normal. The in-plane NV angle is extracted from the B_{NV} bubble image by finding the direction of maximum field gradient at the domain wall and is $16° \pm 2°$ relative to the image x-axis. (b) The simulated magnetic field along the NV axis for the best fit helicity angle 58°. (c) Schematic of the magnetization of a skyrmion bubble with a fixed helicity angle $|\psi_h| = 58°$, viewed from above. The magnetization transitions from pointing upward outside the bubble (red) to pointing downward inside (blue) with a rotation direction between that of Bloch and Néel-type domain walls.

and helicity angle magnitude $|\psi_h|$.

For NV-sample separations larger than Δ_{DW}, a direct measurement of Δ_{DW} is difficult and Δ_{DW} must be inferred from measurements of other parameters. Three parameters are required— M_s, PMA energy density K_{eff}, and domain wall energy density γ_{DW}. The domain wall width is given by $\Delta_{DW} = \sqrt{A_{ex}/K_{eff}}$ [55, 56], corresponding to a magnetization profile across the domain wall $M_z = M_s \tanh(x/\Delta_{DW})$. First $M_s = 6.6 \times 10^5$ A/m and $K_{eff} = 8.3 \times 10^3$ J/m^3 are measured with a SQUID magnetometer. The uncertainty in these parameters is dominated by the unknown magnetic dead-layer thickness [35]. The domain wall energy density can be estimated from the period of the stripe spacing in the NV stripe-phase images, or calculated more directly by comparing the demagnetization energy and total domain wall length in the image area. The exchange stiffness is then calculated from $\gamma_{DW} = 4\sqrt{A_{ex}K_{eff}} - \pi|D| = 1.3$ mJ/m^3, where $D = 47$ μJ/m^2 is the DMI energy density determined from Brillouin light scattering (BLS) measurements [35, 36]. These values give a domain wall width $\Delta_{DW} = 33$ nm. Armed with these parameters, we can compare the expected stray field for a given helicity magnitude to that measured with the scanning NV center.

Figure 6b shows the best-fit simulated stray field corresponding to the measurement stray field in Fig. 4a. The best-fit helicity angle magnitude, $|\psi_h| = 58°$ is determined by minimizing the RMS error between the measured and simulated stray field, as a function of $|\psi_h|$, in a 1.4 μm box centered on the bubble. Values obtained for other skyrmions include $|\psi_h| = 72°$ and 75° [35]. To allow for the possibility that the helicity angle can change locally along the bubble domain wall, it is instructive to compare the simulated stray field as a function of position along the domain wall. In Fig. 6a, linecuts across the measured and simulated field images are shown as a function of cut angle and helicity type. The skyrmion bubbles in this material consistently show a right-handed helicity angle. A constant right-handed helicity is consistent with a non-zero winding number, but it is important to note that uncertainties in sample thickness and NV height will change the measured helicity angle magnitude. The right-handed helicity observed here agrees with BLS measurements of D, but micromagnetic theory gives a smaller magnitude helicity angle based on the bulk material parameters and the measured D [35]. This discrepancy between a bulk calculation and local measurements of the helicity angle may come from spatial fluctuations in the material parameters [17]. For example, we observe variations in the stray field measured in the saturated magnetic state (Fig. S13), which we attribute to variations in the parameter $I_s = M_s t$. The domain wall energy density is lowered in areas where the film is thicker or M_s is larger, and the domain walls will likely be pinned in these areas. Since the helicity angle depends on M_s and t this effect will lead to a different helicity angle calculated from bulk measurements of M_s, t, and D and the helicity angle measured locally at the domain walls.

VI. DISCUSSION AND FUTURE NV STUDIES OF SKYRMIONS

This work extends recently developed scanning NV microscopy techniques used to study multilayer skyrmion materials. Specifically, we have demonstrated that NV microscopy can simultaneously locally probe both magnetic structure and dynamics. As shown in similar thin film systems [29], pinning and disorder are important factors in determining static skyrmion bubble sizes in Ta/CoFeB/MgO. We have shown that these sizes are determined dynamically, via hopping of skymion bubble domain walls between pinning sites. We have also probed the dynamics of these hopping processes and we've observed increased magnetic fluctuations near skyrmion bubble domain walls. Our measurements confirm the right-handed helicity of the DM interaction in this specific material structure and we have measured helicity angle magnitudes in a range $|\psi_h| = 58° - 75°$.

Our images highlight the importance of pinning interactions between defects and the internal degrees of freedom of skyrmion bubbles. As shown previously [9], standard defect-agnostic micromagnetic models of skyrmion motion break down when material inhomogeneities exist on length scales smaller than the skyrmion size. In this work, we experimentally observe the interaction of skyrmion bubbles with these inhomogeneities. This indicates that the behavior of future devices based on the skyrmion bubbles in this material, or similar materials, will be determined by pinning interactions. Specfically, these pinning sites will likely determine the current-driven velocity and trajectory of skyrmion motion [9, 53]. For use in future devices, skyrmions with smaller diameters are desired [13] and aspects of the pinning dynamics investigated here may change as the skyrmion diameter decreases or the DMI strength is increased. However, as the development of multilayer skyrmion material continues, measurements similar to those demonstrated here will provide powerful techniques for the characterization of nanometer-scale skyrmions.

Inspired by this work, a more thorough study of the fluctuation dynamics observed here is a promising direction for future NV-based skyrmion experiments. NV noise spectroscopy has been developed as a powerful tool for obtaining information about the dynamics of noise processes in materials [31, 39, 57–60]. In the future, NV noise spectroscopy could be utilized to study thermal fluctuation dynamics, which are thought to play an important role in the current driven motion of skrymions [61].

ACKNOWLEDGMENTS

We thank Preeti Ovartchaiyapong for diamond fabrication advice and Simon Meynell and Susanne Baumann for helpful discussions. The work at UCSB was supported by an Air Force Office of Scientific Research PECASE award. A portion of the work was done in the UC Santa Barbara nanofabrication facility, part of the NSF funded NNIN network. The authors acknowledge support from the Nanostructures Cleanroom Facility (NCF) at the California NanoSystems Institute (CNSI). The research reported here made use of shared facilities of the UCSB MRSEC (NSF DMR 1720256), a member of the Materials Research Facilities Network (www.mrfn.org). Kang L. Wang acknowledges the support of NSF-1611570. Guoqiang Yu acknowledges the financial support from the National Natural Science Foundation of China [NSFC, Grants No.11874409], the National Natural Science Foundation of China (NSFC)-Science Foundation Ireland (SFI) Partnership Programme [Grant No. 51861135104], and 1000 Youth Talents Program. Xin Ma acknowledges the support from NSF grant CCF 1740352 and SRC nCORE NC-2766-A. The work at UT Austin was primarily supported as part of SHINES, an Energy Frontier Research Center funded by the U.S. Department of Energy (DOE), Office of Science, Basic Energy Science (BES) under

Award No. DE-SC0012670. [35]

[1] S. Mühlbauer, B. Binz, F. Jonietz, C. Pfleiderer, A. Rosch, A. Neubauer, R. Georgii, and P. Böni, "Skyrmion lattice in a chiral magnet," Science **323** (2009).

[2] X Z Yu, N Kanazawa, Y Onose, K Kimoto, W Z Zhang, S Ishiwata, Y Matsui, and Y Tokura, "Near room-temperature formation of a skyrmion crystal in thin-films of the helimagnet FeGe," Nature Materials **10**, 106–109 (2011).

[3] Stefan Heinze, Kirsten Von Bergmann, Matthias Menzel, Jens Brede, André Kubetzka, Roland Wiesendanger, Gustav Bihlmayer, and Stefan Blügel, "Spontaneous atomic-scale magnetic skyrmion lattice in two dimensions," Nature Physics **7**, 713–718 (2011).

[4] T Schulz, R Ritz, A Bauer, M Halder, M Wagner, C Franz, C Pfleiderer, K Everschor, M Garst, and A Rosch, "Emergent electrodynamics of skyrmions in a chiral magnet," Nature Physics **8**, 301–304 (2012).

[5] F. Jonietz, S. Mühlbauer, C. Pfleiderer, A. Neubauer, W. Münzer, A. Bauer, T. Adams, R. Georgii, P. Böni, R. A. Duine, K. Everschor, M. Garst, and A. Rosch, "Spin Transfer Torques in MnSi at Ultralow Current Densities," Science **330** (2010).

[6] J Sampaio, V Cros, S Rohart, A Thiaville, and A Fert, "Nucleation, stability and current-induced motion of isolated magnetic skyrmions in nanostructures," Nature Nanotechnology **8** (2013), 10.1038/NNANO.2013.210.

[7] Albert Fert, Vincent Cros, and Joao Sampaio, "Skyrmions on the track," Nat Nano **8**, 152–156 (2013).

[8] X Z Yu, N Kanazawa, WZ Zhang, T Nagai, T Hara, K Kimoto, Y Matsui, Y Onose, and Y Tokura, "Skyrmion flow near room temperature in an ultralow current density," Nature Communications **3**, 988 (2012).

[9] Seonghoon Woo, Kai Litzius, Benjamin Krüger, Mi Young Im, Lucas Caretta, Kornel Richter, Maxwell Mann, Andrea Krone, Robert M Reeve, Markus Weigand, Parnika Agrawal, Ivan Lemesh, Mohamad Assaad Mawass, Peter Fischer, Mathias Kläui, and Geoffrey S.D. Beach, "Observation of room-temperature magnetic skyrmions and their current-driven dynamics in ultrathin metallic ferromagnets," Nature Materials **15**, 501–506 (2016).

[10] Guoqiang Yu, Pramey Upadhyaya, Xiang Li, Wenyuan Li, Se Kwon Kim, Yabin Fan, Kin L. Wong, Yaroslav Tserkovnyak, Pedram Khalili Amiri, and Kang L. Wang, "Room-Temperature Creation and SpinOrbit Torque Manipulation of Skyrmions in Thin Films with Engineered Asymmetry," Nano Letters **16**, 1981–1988 (2016).

[11] C Moreau-Luchaire, C Moutafis, N Reyren, J Sampaio, C. A.F. Vaz, N. Van Horne, K Bouzehouane, K Garcia, C Deranlot, P Warnicke, P Wohlhüter, J. M. George, M Weigand, J Raabe, V Cros, and A Fert, "Additive interfacial chiral interaction in multilayers for stabilization of small individual skyrmions at room temperature," Nature Nanotechnology **11**, 444–448 (2016).

[12] Anjan Soumyanarayanan, M Raju, A. L.Gonzalez Oyarce, Anthony K.C. Tan, Mi Young Im, A. P. Petrovic, Pin Ho, K H Khoo, M Tran, C K Gan, F Ernult, and C Panagopoulos, "Tunable room-temperature magnetic skyrmions in Ir/Fe/Co/Pt multilayers," Nature Materials **16**, 898–904 (2017).

[13] Albert Fert, Nicolas Reyren, and Vincent Cros, "Magnetic skyrmions: Advances in physics and potential applications," (2017).

[14] Wanjun Jiang, Xichao Zhang, Guoqiang Yu, Wei Zhang, Xiao Wang, M. Benjamin Jungfleisch, John E Pearson, Xuemei Cheng, Olle Heinonen, Kang L Wang, Yan Zhou, Axel Hoffmann, and Suzanne G.E. Te Velthuis, "Direct observation of the skyrmion Hall effect," Nature Physics **13**, 162–169 (2017).

[15] X Z Yu, Y Onose, N Kanazawa, J H Park, J H Han, Y Matsui, N Nagaosa, and Y Tokura, "Real-space observation of a two-dimensional skyrmion crystal," Nature **465**, 901–904 (2010).

[16] Shawn D Pollard, Joseph A Garlow, Jiawei Yu, Zhen Wang, Yimei Zhu, and Hyunsoo Yang, "Observation of stable Néel skyrmions in cobalt/palladium multilayers with Lorentz transmission electron microscopy," Nature Communications **8** (2017), 10.1038/ncomms14761.

[17] K. Zeissler, M. Mruczkiewicz, S. Finizio, J. Raabe, P. M. Shepley, A. V. Sadovnikov, S. A. Nikitov, K. Fallon, S. McFadzean, S. McVitie, T. A. Moore, G. Burnell, and C. H. Marrows, "Pinning and hysteresis in the field dependent diameter evolution of skyrmions in Pt/Co/Ir superlattice stacks," Scientific Reports **7**, 15125 (2017).

[18] Roméo Juge, Soong Geun Je, Dayane de Souza Chaves, Stefania Pizzini, Liliana D. Buda-Prejbeanu, Lucia Aballe, Michael Foerster, Andrea Locatelli, Tevfik Onur Mente, Alessandro Sala, Francesco Maccherozzi, Sarnjeet S. Dhesi, Stéphane Auffret, Eric Gautier, Gilles Gaudin, Jan Vogel, and Olivier Boulle, "Magnetic skyrmions in confined geometries: Effect of the magnetic field and the disorder," Journal of Magnetism and Magnetic Materials **455**, 3–8 (2018).

[19] A. Yagil, A. Almoalem, Anjan Soumyanarayanan, Anthony K. C. Tan, M. Raju, C. Panagopoulos, and O. M. Auslaender, "Stray field signatures of Néel textured skyrmions in Ir/Fe/Co/Pt multilayer films," Applied Physics Letters **112**, 192403 (2018).

[20] M. Baćani, M. A. Marioni, J. Schwenk, and H. J. Hug, "How to measure the local Dzyaloshinskii Moriya Interaction in Skyrmion Thin Film Multilayers," arXiv , 1611.00673 (2016).

[21] J. M. Taylor, P. Cappellaro, L. Childress, L. Jiang, D. Budker, P. R. Hemmer, A. Yacoby, R. Walsworth, and M. D. Lukin, "High-sensitivity diamond magnetometer with nanoscale resolution," Nature Physics **4**, 810–816 (2008).

[22] C. L. Degen, "Scanning magnetic field microscope with a diamond single-spin sensor," Applied Physics Letters **92**, 243111 (2008).

[23] Gopalakrishnan Balasubramanian, I. Y. Chan, Roman Kolesov, Mohannad Al-Hmoud, Julia Tisler, Chang Shin, Changdong Kim, Aleksander Wojcik, Philip R. Hemmer, Anke Krueger, Tobias Hanke, Alfred Leitenstorfer, Rudolf Bratschitsch, Fedor Jelezko, and Jörg Wrachtrup,

"Nanoscale imaging magnetometry with diamond spins under ambient conditions," Nature **455**, 648–651 (2008).
[24] P Maletinsky, S Hong, M S Grinolds, B Hausmann, M D Lukin, R L Walsworth, M Loncar, and A Yacoby, "A robust scanning diamond sensor for nanoscale imaging with single nitrogen-vacancy centres," Nature Nanotechnology **7**, 320–324 (2012).
[25] L Rondin, J. P. Tetienne, S Rohart, A Thiaville, T Hingant, P Spinicelli, J. F. Roch, and V Jacques, "Stray-field imaging of magnetic vortices with a single diamond spin," Nature Communications **4** (2013), 10.1038/ncomms3279.
[26] Y. Dovzhenko, F. Casola, S. Schlotter, T. X. Zhou, F. Büttner, R. L. Walsworth, G. S. D. Beach, and A. Yacoby, "Magnetostatic twists in room-temperature skyrmions explored by nitrogen-vacancy center spin texture reconstruction," Nature Communications **9**, 2712 (2018).
[27] I. Gross, L. J. Martínez, J.-P. Tetienne, T. Hingant, J.-F. Roch, K. Garcia, R. Soucaille, J. P. Adam, J.-V. Kim, S. Rohart, A. Thiaville, J. Torrejon, M. Hayashi, and V. Jacques, "Direct measurement of interfacial Dzyaloshinskii-Moriya interaction in X—CoFeB—MgO heterostructures with a scanning NV magnetometer (X=Ta, TaN, and W)," Physical Review B **94**, 064413 (2016).
[28] Matthew Pelliccione, Alec Jenkins, Preeti Ovartchaiyapong, Christopher Reetz, Eve Emmanouilidou, Ni Ni, and Ania C Bleszynski Jayich, "Scanned probe imaging of nanoscale magnetism at cryogenic temperatures with a single-spin quantum sensor," Nature Nanotechnology **11**, 700–705 (2016).
[29] I. Gross, W. Akhtar, A. Hrabec, J. Sampaio, L. J. Martínez, S. Chouaieb, B. J. Shields, P. Maletinsky, A. Thiaville, S. Rohart, and V. Jacques, "Skyrmion morphology in ultrathin magnetic films," Physical Review Materials **024406**, 1–6 (2018).
[30] Felix Büttner, Ivan Lemesh, and Geoffrey S.D. Beach, "Theory of isolated magnetic skyrmions: From fundamentals to room temperature applications," Scientific Reports **8** (2018), 10.1038/s41598-018-22242-8.
[31] Toeno van der Sar, Francesco Casola, Ronald Walsworth, and Amir Yacoby, "Nanometre-scale probing of spin waves using single electron spins," Nature Communications **6**, 7886 (2015).
[32] S. Dreyer, J. Norpoth, C. Jooss, S. Sievers, U. Siegner, V. Neu, and T. H. Johansen, "Quantitative imaging of stray fields and magnetization distributions in hard magnetic element arrays," Journal of Applied Physics **101** (2007), 10.1063/1.2717560.
[33] Eduardo A. Lima and Benjamin P. Weiss, "Obtaining vector magnetic field maps from single-component measurements of geological samples," Journal of Geophysical Research: Solid Earth **114** (2009), 10.1029/2008JB006006.
[34] J. P. Tetienne, T Hingant, L J Martínez, S Rohart, A Thiaville, L. Herrera Diez, K Garcia, J. P. Adam, J. V. Kim, J. F. Roch, I M Miron, G Gaudin, L Vila, B Ocker, D Ravelosona, and V Jacques, "The nature of domain walls in ultrathin ferromagnets revealed by scanning nanomagnetometry," Nature Communications **6** (2015), 10.1038/ncomms7733.
[35] See Supplemental Material [url] for information on material parameters, calibrations, and magnetization reconstruction, which includes Refs. [62–67].
[36] Xin Ma, Guoqiang Yu, Xiang Li, Tao Wang, Di Wu, Kevin S. Olsson, Zhaodong Chu, Kyongmo An, John Q. Xiao, Kang L. Wang, and Xiaoqin Li, "Interfacial control of Dzyaloshinskii-Moriya interaction in heavy metal/ferromagnetic metal thin film heterostructures," Physical Review B **94**, 180408(R) (2016).
[37] Xin Ma, Guoqiang Yu, Seyed A. Razavi, Stephen S. Sasaki, Xiang Li, Kai Hao, Sarah H. Tolbert, Kang L. Wang, and Xiaoqin Li, "Dzyaloshinskii-Moriya Interaction across an Antiferromagnet-Ferromagnet Interface," Physical Review Letters **119**, 027202 (2017).
[38] Xin Ma, Guoqiang Yu, Chi Tang, Xiang Li, Congli He, Jing Shi, Kang L. Wang, and Xiaoqin Li, "Interfacial Dzyaloshinskii-Moriya Interaction: Effect of 5d Band Filling and Correlation with Spin Mixing Conductance," Physical Review Letters **120**, 157204 (2018).
[39] B. A. Myers, A. Das, M. C. Dartiailh, K. Ohno, D. D. Awschalom, and A. C. Bleszynski Jayich, "Probing surface noise with depth-calibrated spins in diamond," Physical Review Letters **113**, 027602 (2014).
[40] A. A. Thiele, "Theory of the static stability of cylindrical domains in uniaxial platelets," Journal of Applied Physics **41**, 1139–1145 (1970).
[41] M. Eltschka, M. Wötzel, J. Rhensius, S. Krzyk, U. Nowak, M. Kläui, T. Kasama, R. E. Dunin-Borkowski, L. J. Heyderman, H. J. van Driel, and R. A. Duine, "Nonadiabatic Spin Torque Investigated Using Thermally Activated Magnetic Domain Wall Dynamics," Physical Review Letters **105**, 056601 (2010).
[42] N. Bloembergen, E. M. Purcell, and R. V. Pound, "Relaxation Effects in Nuclear Magnetic Resonance Absorption," Physical Review **73**, 679–712 (1948).
[43] J. Li, M. P. Silveri, K. S. Kumar, J. M. Pirkkalainen, A. Vepsäläinen, W. C. Chien, J. Tuorila, M. A. Sillanpää, P. J. Hakonen, E. V. Thuneberg, and G. S. Paraoanu, "Motional averaging in a superconducting qubit," Nature Communications **4**, 1420 (2013).
[44] M. Kronseder, T. N.G. Meier, M. Zimmermann, M. Buchner, M. Vogel, and C. H. Back, "Real-time observation of domain fluctuations in a two-dimensional magnetic model system," Nature Communications **6**, 6832 (2015).
[45] J. P. Tetienne, T Hingant, J. V. Kim, L. Herrera Diez, J. P. Adam, K Garcia, J. F. Roch, S Rohart, A Thiaville, D Ravelosona, and V Jacques, "Nanoscale imaging and control of domain-wall hopping with a nitrogen-vacancy center microscope," Science **344**, 1366–1369 (2014).
[46] M Mochizuki, X Z Yu, S Seki, N Kanazawa, W Koshibae, J Zang, M Mostovoy, Y. Tokura, and N. Nagaosa, "Thermally driven ratchet motion of a skyrmion microcrystal and topological magnon Hall effect," Nature Materials **13**, 241–246 (2014).
[47] K Wagner, A Kákay, K. Schultheiss, A Henschke, T Sebastian, and H Schultheiss, "Magnetic domain walls as reconfigurable spin-wave nanochannels," Nature Nanotechnology **11**, 432–436 (2016).
[48] S Rohart, J Miltat, and A Thiaville, "Path to collapse for an isolated N\'eel skyrmion," PHYSICAL REVIEW B **93**, 214412 (2016).
[49] Xiuzhen Yu, Daisuke Morikawa, Tomoyuki Yokouchi, Kiyou Shibata, Naoya Kanazawa, Fumitaka Kagawa, Taka hisa Arima, and Yoshinori Tokura, "Aggregation and collapse dynamics of skyrmions in a non-equilibrium

state," Nature Physics **14**, 832–836 (2018).

[50] J. A. Cape and G. W. Lehman, "Magnetic domain structures in thin uniaxial plates with perpendicular easy axis," Journal of Applied Physics **42**, 5732–5756 (1971).

[51] A Neubauer, C Pfleiderer, B Binz, A Rosch, R Ritz, P G Niklowitz, and P Böni, "Topological Hall effect in the A-phase of MnSi," Physical Review Letters **102**, 186602 (2009).

[52] R. Tomasello, E. Martinez, R. Zivieri, L. Torres, M. Carpentieri, and G. Finocchio, "A strategy for the design of skyrmion racetrack memories," Scientific Reports **4**, 6784 (2014).

[53] Kai Litzius, Ivan Lemesh, Benjamin Krüger, Pedram Bassirian, Lucas Caretta, Kornel Richter, Felix Büttner, Koji Sato, Oleg A. Tretiakov, Johannes Förster, Robert M. Reeve, Markus Weigand, Iuliia Bykova, Hermann Stoll, Gisela Schütz, Geoffrey S.D. Beach, and Mathias Klaüi, "Skyrmion Hall effect revealed by direct time-resolved X-ray microscopy," Nature Physics **13**, 170–175 (2017).

[54] T. Hingant, J. P. Tetienne, L. J. Martínez, K. Garcia, D. Ravelosona, J. F. Roch, and V. Jacques, "Measuring the magnetic moment density in patterned ultrathin ferromagnets with submicrometer resolution," Physical Review Applied **4**, 014003 (2015).

[55] S. Rohart and A. Thiaville, "Skyrmion confinement in ultrathin film nanostructures in the presence of Dzyaloshinskii-Moriya interaction," Physical Review B **88**, 184422 (2013).

[56] T. N.G. Meier, M. Kronseder, and C. H. Back, "Domain-width model for perpendicularly magnetized systems with Dzyaloshinskii-Moriya interaction," Physical Review B **96**, 144408 (2017).

[57] Kartiek Agarwal, Richard Schmidt, Bertrand Halperin, Vadim Oganesyan, Gergely Zaránd, Mikhail D. Lukin, and Eugene Demler, "Magnetic noise spectroscopy as a probe of local electronic correlations in two-dimensional systems," Physical Review B **95**, 155107 (2017).

[58] B. A. Myers, A. Ariyaratne, and A. C. Bleszynski Jayich, "Double-Quantum Spin-Relaxation Limits to Coherence of Near-Surface Nitrogen-Vacancy Centers," Physical Review Letters **118**, 197201 (2017).

[59] G. de Lange, Z. H. Wang, D. Ristè, V. V. Dobrovitski, and R. Hanson, "Universal dynamical decoupling of single solid spin from spin bath," Science **330** (2010).

[60] Chunhui Du, Toeno van der Sar, Tony X Zhou, Pramey Upadhyaya, Francesco Casola, Huiliang Zhang, Mehmet C Onbasli, Caroline A Ross, Ronald L Walsworth, Yaroslav Tserkovnyak, and Amir Yacoby, "Control and local measurement of the spin chemical potential in a magnetic insulator," Science **357**, 195–198 (2017).

[61] Roberto E. Troncoso and Alvaro S. Núñez, "Thermally assisted current-driven skyrmion motion," Physical Review B - Condensed Matter and Materials Physics **89**, 224403 (2014).

[62] M T. Johnson, P J H. Bloemen, F J A. den Broeder, and J J. de Vries, "Magnetic anisotropy in metallic multilayers," Rep. Prog. Phys **59**, 1409–1458 (1996).

[63] Soo Young Jang, S. H. Lim, and S. R. Lee, "Magnetic dead layer in amorphous CoFeB layers with various top and bottom structures," Journal of Applied Physics **107**, 09C707 (2010).

[64] Jaivardhan Sinha, Masamitsu Hayashi, Andrew J. Kellock, Shunsuke Fukami, Michihiko Yamanouchi, Hideo Sato, Shoji Ikeda, Seiji Mitani, See Hun Yang, Stuart S. P. Parkin, and Hideo Ohno, "Enhanced interface perpendicular magnetic anisotropy in Ta—CoFeB—MgO using nitrogen doped Ta underlayers," Applied Physics Letters **102**, 242405 (2013).

[65] Benjamin Buford, Pallavi Dhagat, and Albrecht Jander, "Estimating exchange stiffness of thin films with perpendicular anisotropy using magnetic domain images," IEEE Magnetics Letters **7**, 1–5 (2016).

[66] M J. Donahue and D G. Porter, *OOMMF User's Guide, Version 1.0*, Tech. Rep. (NIST, 1999).

[67] Niculin Andri Saratz, *Inverse Symmetry Breaking in Low-Dimensional Systems*, Ph.D. thesis (2010).